NH$_3$ observations of the S235 star-forming region: Dense gas in inter-core bridges

Ross A. BURNS,[1,2,3,4,*] **Toshihiro HANDA,**[5,*] **Toshihiro OMODAKA,**[4,*]
Andrej M. SOBOLEV,[6] **Maria S. KIRSANOVA,**[6,7,8] **Takumi NAGAYAMA,**[9]
James O. CHIBUEZE,[10,11] **Mikito KOHNO,**[12] **Makoto NAKANO,**[13]
Kazuyoshi SUNADA,[9] **and Dmitry A. LADEYSCHIKOV**[6]

[1]Mizusawa VLBI Observatory, National Astronomical Observatory of Japan, 2-21-1 Osawa, Mitaka, Tokyo 181-8588, Japan

[2]Korea Astronomy and Space Science Institute, 776 Daedeokdae-ro, Yuseong-gu, Daejeon, 34055, Republic of Korea

[3]Joint Institute for VLBI ERIC, Oude Hoogeveensedijk 4, 7991 PD Dwingeloo, the Netherlands

[4]Graduate School of Science and Engineering, Kagoshima University, 1-21-35 Kôrimoto, Kagoshima, Kagoshima 890-0065, Japan

[5]Amanogawa Galaxy Astronomy Research Center, Kagoshima University, 1-21-35 Kôrimoto, Kagoshima, Kagoshima 890-0065, Japan

[6]Ural Federal University, 19 Mira St. 620002, Ekaterinburg, Russia

[7]Institute of Astronomy, Russian Academy of Sciences, 48 Pyatnitskaya Str. 119017, Moscow, Russia

[8]Moscow Institute of Physics and Technology, 141701, 9 Institutskiy per., Dolgoprudny, Moscow Region, Russia

[9]Mizusawa VLBI observatory, NAOJ 2-12, Hoshigaoka, Mizusawa, Oshu, Iwate 023-0861, Japan

[10]Space Research Unit, Physics Department, North-West University, Potchefstroom, 2520, South Africa

[11]Department of Physics and Astronomy, University of Nigeria, Carver Building, 1 University Road, Nsukka, 410001, Nigeria

[12]Department of Physics, Nagoya University, Furo-cho, Chikusa-ku, Nagoya, Aichi 464-8601, Japan

[13]Faculty of Science and Technology, Oita University, 700 Dannoharu, Oita, Oita 870-1192, Japan

*E-mail: ross.burns@nao.ac.jp (RAB), Handa@sci.kagoshima-u.ac.jp (TH), Omodaka@sci.kagoshima-u.ac.jp (TO)

Abstract

Star formation is thought to be driven by two groups of mechanisms; spontaneous collapse and triggered collapse. Triggered star formation mechanisms further diverge into cloud–cloud collision (CCC), "collect and collapse" (C&C) and shock-induced collapse of pre-existing, gravitationally stable cores, or "radiation driven implosion" (RDI). To evaluate the contributions of these mechanisms and establish whether these processes can occur together within the same star-forming region, we performed mapping observations of radio-frequency ammonia and water maser emission lines in the S235 massive star-forming region. Via spectral analyses of main, hyperfine, and multi-transitional ammonia lines we explored the distribution of temperature and column density in the dense gas in the S235 and S235AB star-forming region. The most remarkable result of the mapping observations is the discovery of high-density gas in inter-core bridges which physically

link dense molecular cores that house young proto-stellar clusters. The presence of dense gas implies the potential for future star formation within the system of cores and gas bridges. Cluster formation implies collapse, and the continuous physical links, also seen in re-imaged archival CS and ^{13}CO maps, suggest a common origin to the molecular cores housing these clusters, i.e a structure condensed from a single, larger parent cloud, brought about by the influence of a local expanding H II region. An ammonia absorption feature co-locating with the center of the extended H II region may be attributed to an older gas component left over from the period prior to formation of the H II region. Our observations also detail known and new sites of water maser emission, highlighting regions of active ongoing star formation.

Key words: ISM: molecules — stars: formation — stars: individual (S235)

1 Introduction

The existence of Galactic-scale star formation relations such as the Kennicut–Schmidt law (Schmidt 1959; Kennicutt 1998) implies continuity in star formation activity at all scales; from individual (proto-)stars ($<10^1$ pc), to local star-forming region (SFR) scales (10^{1-2} pc), to Galactic-scale star formation ($>10^2$ pc); see, for example Nguyen-Luong et al. (2016). At an intermediate between the Galactic and (proto-)star scales, investigations on the scale of individual SFRs are required for completeness; to link our knowledge of star formation across all scales.

At SFR scales, star formation is thought to be driven by two groups of mechanisms; spontaneous collapse and triggered collapse (Elmegreen & Lada 1977; Elmegreen 1998). Spontaneous collapse is the case when a super-critical density gas cloud is allowed to contract gravitationally, relatively undisturbed, while triggered collapse pertains to an external influence which encourages collapse by compressing sub-critical gas beyond critical density. Triggered star formation mechanisms further diverge into "collect and collapse" (C&C) (Elmegreen & Lada 1977), shock-induced collapse of pre-existing, gravitationally stable cores, or "radiation driven implosion" (RDI) (Sandford et al. 1982) and large scale cloud–cloud collisions (CCCs) capable of generating the widespread over-densities required to drive sequential star formation (Habe & Ohta 1992; Haworth et al. 2015a, 2015b, 2018; Torii et al. 2017).

The ammonia molecule has long been recognized as a sensitive thermometer and densitometer for probing the interstellar medium (Ho & Townes 1983; Walmsley 1994). It has been used extensively to probe physical conditions in various stages of star formation including pre-stellar cores (Ruoskanen et al. 2011), active star formation cores (Harju et al. 1991; Kirsanova et al. 2014; Ladeyschikov et al. 2016), filamentary structures (Wu et al. 2018), and large-scale star formation surveys (Friesen et al. 2017).

Several recent works by our group have used ammonia mapping observations to look for evidence of spontaneous and triggered star formation (Toujima et al. 2011; Chibueze et al. 2013; Nakano et al. 2017), with the goal of uncovering which mechanism is dominant and whether these processes can occur together within the same star-forming region. As a continuation of this project, we conducted radio-frequency ammonia transition mapping observations of the S235 "main" and S235AB (collectively termed "S235" hereafter) star-forming region with the goal of mapping the physical conditions of molecular gas.

S235 is the most active region of star formation of the G174+2.5 giant molecular cloud. It houses multiple dense gas cores which have been extensively studied using NH_3, CS, and ^{13}CO molecular lines (Kirsanova et al. 2008, 2014). However, previous NH_3 maps of S235 were exclusive to the well-known dense cores and did not sample the regions between or around the cores. More complete observations were made by Dewangan and Ojha (2017) using CO and its isotopologues, thus tracing the widespread diffuse gas. Regarding continuum emission, S235 is home to a circular H II region driven by ionizing radiation from an O9.5 V star, (BD +35°1201) (Georgelin et al. 1973), at the center of the H II region. Dewangan and Anandarao (2011) report that stellar densities of young stellar objects (YSOs) in S235 concentrate in the four molecular cores which are referred to as East1, East2, Central-West, and Central-East in Kirsanova et al. (2008, 2014). In this work we adopt their notation and use short-hands E1, E2, CW, and CE, respectively. Kirsanova et al. (2008, 2014) suggest that the molecular cores may have formed via the C&C mechanism through interaction with the H II region. More recently, work by Dewangan et al. (2016) added support to this picture by showing with high confidence that star formation in S235 is driven by interaction with the expanding H II, as is the conclusion of their thorough multi-wavelength investigation. Dewangan and Ojha (2017) further revealed evidence of a past CCC event which likely initiated the subsequent star formation observed today.

Further to the south, the S235AB region is home to a younger H II region, S235A, and very intense star formation indicated by high concentrations of YSOs (Dewangan & Anandarao 2011). Maser activity in this region also points to the presence of very young massive star formation (Felli et al. 2007; Burns et al. 2015), and enabled the distance to S235 to be established as $D_\pi = 1.56^{+0.09}_{-0.08}$ kpc, via maser parallax (Burns et al. 2015). The combined presence of molecular cores, H II regions, and star formation at various evolutionary stages makes S235 an ideal region to investigate various scenarios pertaining to spontaneous and triggered star formation.

2 Observations and archival data

Observations of S235 were carried out between 2013 December and 2014 June using the Nobeyama 45-m radio telescope, operated by the Nobeyama Radio Observatory (NRO), a branch of the National Astronomical Observatory of Japan (NAOJ). The telescope was operated in the single side-band mode with frequency windows centered at the rest frequencies of NH_3 inversion transitions $(J, K) = (1, 1), (2, 2)$, and $(3, 3)$ at 22.6914, 23.722, and 23.870 GHz, respectively, and the H_2O $6_{12} - 5_{23}$ maser transition at 22.235 GHz. All frequency bands were observed simultaneously with dual linear polarizations and autocorrelated with a 0.38 km s^{-1} velocity channel spacing. The FWHM beamsize was 75″, pointing was checked every 1–2 hours, and deviations were kept below 5″.

Mapping observations were conducted in position switching mode (ON–OFF) using map grid spacings of 37″.5. Sky subtraction was achieved by observing a region with no emission. Repeated integrations of 20 s were made at each point, with three ON points for every OFF point.

T_{sys} varied between $T_{sys} = 90$–140 K for all observing runs, thus scans were integrated until an rms noise level of 0.04 K was reached for each mosaic point. This provided an overall consistency in map noise irrespective of the changing T_{sys}. Maps were created sequentially, beginning at the coordinates of the dense gas cores described in the literature (E1, E2, Central, AB) and extending outwards from those cores until no emission was detected. It is possible that ammonia emission existing between the S235 complex and S235AB was missed. Confirmation should be made by further observations. The total observing time required to produce the final maps of the S235 and S235AB regions was 120 hr.

Data reduction was performed using the NEWSTAR software, which has been developed and maintained by NRO. Baseline subtraction was performed individually for all scans, frequency bands, and polarizations, after which polarizations were combined to Stokes I. Fitting and analyses of the molecular inversion spectrum of ammonia were carried out with *gnuplot* routines which parametrized the main line and satellite line profiles. Non-detections (grey squares in the emission maps) were recorded lacking a 2σ detection.

3 Results

3.1 Ammonia: Emission maps

Maps of the ammonia $(1, 1)$, $(2, 2)$, and $(3, 3)$ emission in S235 are shown in figure 1 where the reference coordinate $(0, 0)$ corresponds to $(\alpha, \delta)_{J2000.0} = (05^h41^m33^s.8, +35°48'27'')$. Ammonia from the $(1, 1)$ transition was detected in our observations at all cores, the regions between the cores, and in S235AB. Emission from the $(2, 2)$ transition was seen in the four cores and S235AB
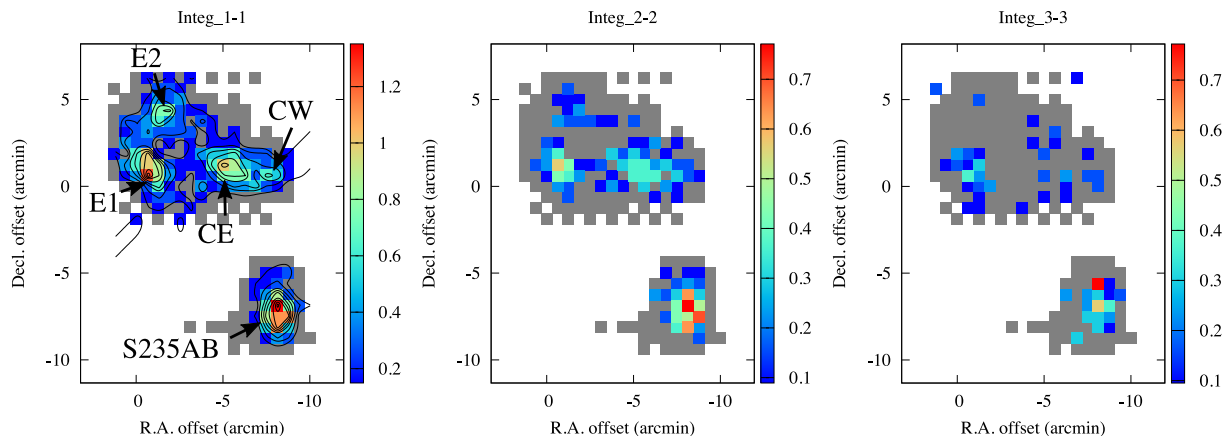
Fig. 1. Maps of the ammonia in S235 and S235AB, showing (from left to right) the intensities of the $(1, 1)$, $(2, 2)$, and $(3, 3)$ emission. Colour scales indicate brightness temperatures in units of kelvin, scaled individually for each map. Grey squares indicate no emission at or above the 2σ cut-off. Contours in the $(1, 1)$ map increase from three times the rms noise in integer intervals. (Color online)
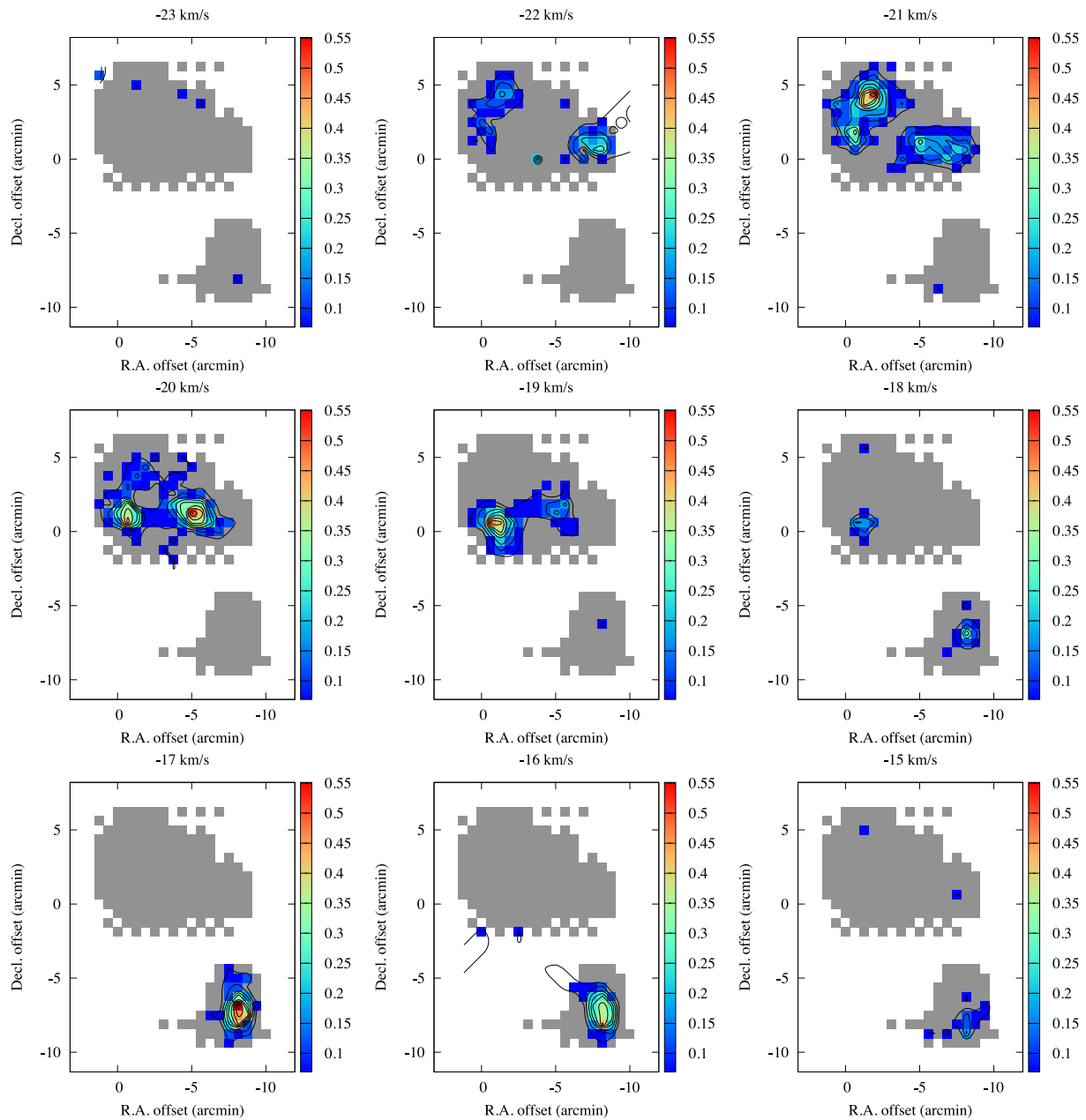
Fig. 2. Channel maps of the ammonia (1, 1) emission in S235 and S235AB. Colour scales indicate brightness temperatures in units of kelvin, scaled individually for each map. Contours in the (1, 1) map increase from three times the rms noise in integer intervals. Grey squares indicate no emission at or above the 2σ cutoff. (Color online)

but was rarely detected in the inter-core regions. Emission from the $(3, 3)$ transition was primarily detected in E1 and S235AB.

Channel maps of integer increment are shown in figure 2. Core and inter-core gasses are continuous in velocity, with emission velocities ranging from -15 to $-21\,\mathrm{km\,s^{-1}}$ (figure 3). Thus the majority of emission is seen to be blueshifted with respect to the ambient molecular cloud at $-17\,\mathrm{km\,s^{-1}}$ (Heyer et al. 1996). Velocity widths of the ammonia spectra are in the range of 1 to $3\,\mathrm{km\,s^{-1}}$.

3.2 Deriving physical parameters of molecular gas

To derive the physical conditions of the ammonia gas in our mapped regions, we first calculate the optical depth, τ, using the ratio of integrated main and satellite line temperatures:

$$\frac{T_{MB}(\text{main})}{T_{MB}(\text{satellite})} = \frac{1 - e^{-\tau}}{1 - e^{-a\tau}}, \tag{1}$$

where a is the natural intensity ratio of the satellite to main lines. We then calculate the rotation temperature of the gas,
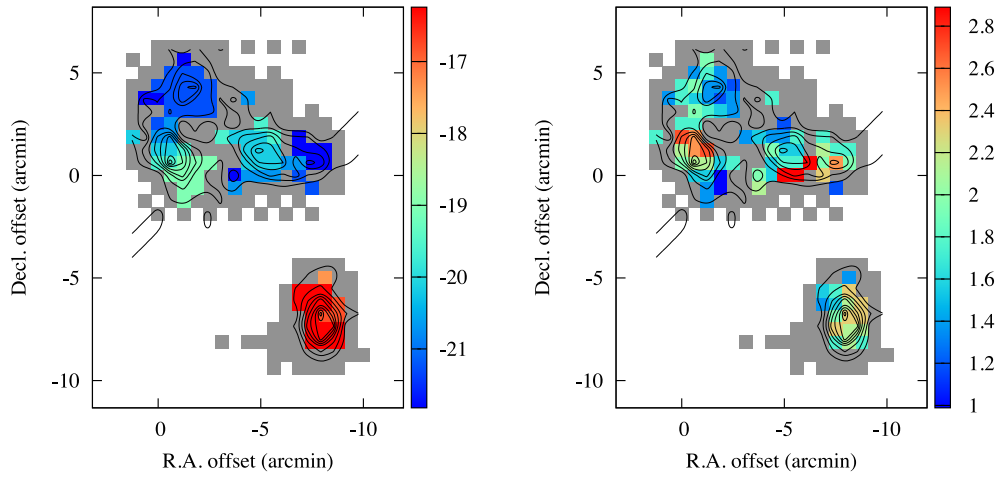
Fig. 3. The first and second moment maps of ammonia in S235 (left) and S235AB (right). Colour scales are in units of km s^{-1}. Overlain contours outline the ammonia (1,1) intensity profile from figure 1. (Color online)

$T_{\rm rot}$, using

$$T_{\rm rot} = -41.5 /$$
$$\ln \left\{ \frac{-0.282}{\tau} \ln \left[1 - \frac{T_{MB}(2, 2)}{T_{MB}(1, 1)} (1 - e^{-\tau}) \right] \right\}. \quad (2)$$

The column density of gas emitting at the (J, K) transition, $N(J, K)$, is calculated using

$$N(1, 1) = A \times 10^{13} \tau(J, K, main) T_{\rm rot} \Delta v_{1/2}, \quad (3)$$

where A in this case is a dimensionless constant corresponding to $A = 2.78, 1.31, 1.03$ for $(J, K) = (1, 1)$, $(2, 2)$, $(3, 3)$, respectively. Finally, the total NH$_3$ column density, $N_{\rm TOT}$, is calculated assuming local thermodynamic equilibrium, using

$$N_{\rm TOT} = \frac{N(J, K)}{g_J, g_I, g_K} \exp \left[\frac{E(J, K)}{T_{\rm rot}} \right]$$
$$\Sigma g_J, g_I, g_K \exp \left[\frac{-E_i(J, K)}{T_{\rm rot}} \right], \quad (4)$$

where g_J is the rotational degeneracy, g_I is the nuclear spin degeneracy, and g_K is the K-degeneracy.

3.3 Ammonia: Mapping the physical conditions of molecular gas in S235

Based on the relations described in subsection 3.2, we estimated the physical conditions of ammonia gas at each point in the grid. Since only a few map positions had sufficiently bright satellite emission for deriving the gas opacity, we adopt the average value of τ for each core for the subsequent calculations of $T_{\rm rot}$ and $N_{\rm TOT}$ at each map point in S235 and S235AB. Maps of these parameters are shown in figure 4.

We then evaluated further physical parameters (gas opacity, τ; rotational temperature, $T_{\rm rot}$; velocity width, Δv; total gas column density, N_{H_2}; and core mass, $M_{\rm LTE}$) associated with cores E1, E2, CW, CE, and S235AB. For this step we employed an ammonia abundance ratio of $X(\rm NH_3) = 1.379 \times 10^{-7}$, following Millar et al. (1997). Physical parameters for cores were reached by integrating over their angular area, based on their sizes given in Kirsanova et al. (2014). These are reported in table 1.

3.4 CS and ^{13}CO: Re-imaging archival maps

In order to compare the results of our ammonia mapping observations with the distributions of gasses at other densities, we revisited the CS(2–1) and ^{13}CO(1–0) data of Kirsanova et al. (2008). The maps, made with the Onsala 20-m telescope, have full width at half-maximum (FWHM) beamsizes of 34″ and 38″ for the CS and ^{13}CO data, respectively, producing maps of almost equal angular resolution to those of the ammonia grid spacings taken at Nobeyama. The reader may refer to the aforementioned publication for further details of the observations. Channel maps were produced at integer velocity intervals; these are shown in figures 5 and 6.

3.5 Inter-core gas bridges: physical parameters

From figure 1 it is apparent that an extended gas component of ammonia was detected in the regions outside of the main cores apparently forming a network of inter-core bridges. Withholding a deeper discussion of these gas bridges for section 4, in this section we derive the physical parameters of gas belonging to this component.
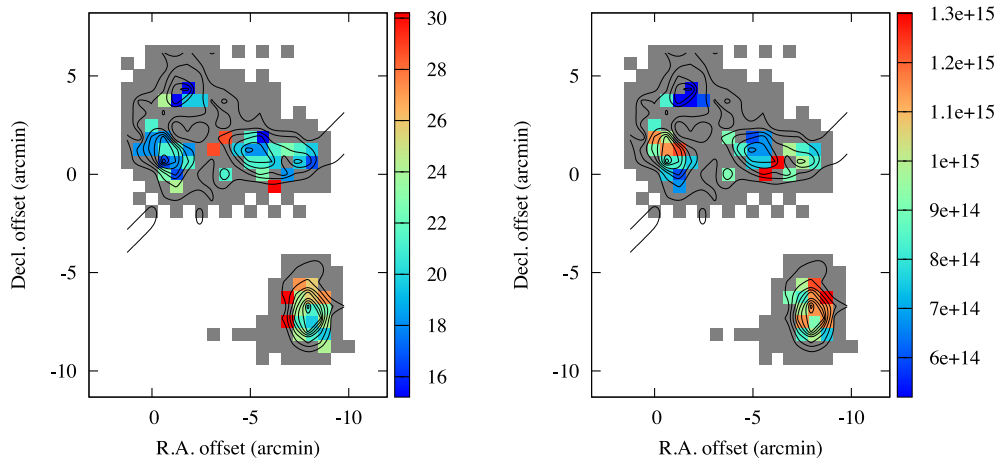
Fig. 4. Maps of the physical gas parameters in S235 and S235AB. Left: Rotational temperature, $T_{\rm rot}$, of ammonia in which the colour scale indicates temperatures in kelvin. Right: Total column density, $N_{\rm TOT}$, of ammonia gas in units of cm^{-2}. (Color online)

Table 1. Physical conditions of the star-forming cores in S235.

Name	τ [K]	$T_{\rm rot}$	$\Delta\nu$ [km s^{-1}]	N_{H_2} [cm^{-2}]	$M_{\rm LTE}$ [$M_\odot$]
East 1	0.28 ± 0.32	19 ± 1	1.75 ± 0.47	(8.7 ± 1.8) × 10^{21}	138 ± 11
East 2	0.41 ± 0.53	18 ± 2	1.56 ± 0.23	(10.6 ± 1.5) × 10^{21}	55 ± 6
Central E	0.62 ± 0.46	20 ± 2	1.77 ± 0.41	(1.9 ± 0.4) × 10^{21}	152 ± 12
Central W	1.43 ± 0.56	20 ± 1	2.08 ± 0.37	(5.4 ± 0.7) × 10^{21}	101 ± 9
S235AB	0.08 ± 0.23	23 ± 1	1.94 ± 0.31	(3.2 ± 0.4) × 10^{21}	276 ± 26

Ammonia emission from the "inter-core" gas was too weak to analyse on a point-by-point basis. We therefore integrated signals from all pointings considered to be inter-core gas by the definition of being outside the derived core radii listed in table 1. Since inter-core gas exhibits little to no star formation activity, no large velocity widths, and no gradients, such an integration can be considered reliable. Integrated spectra of the ammonia (1, 1) and (2, 2) from inter-core gas are shown in figure 7.

Repeating the spectral analyses outlined in section 3 we derived the physical properties of the inter-core gas in S235. For this gas component we estimated an optical depth of $\tau = 0.12 \pm 0.43$, rotation temperature of $T_{\rm rot} = 18.01 \pm 3.78$ K, and a total gas column density of $N_{H_2} = 1.3 \pm 4.8 \times 10^{21}$ cm^{-2}. Assuming that the gas bridges are of equal depth as their width (0.4 pc), the density of gas in the gas bridges would be $\rho = 1.1 \pm 4.1 \times 10^3$ cm^{-3}.

Filamentary clouds become unstable when the line mass per unit length exceeds the critical line mass, i.e., $M_{\rm line} > M_{\rm crit}$ [see Inutsuka and Miyama (1997) and, for example, Ryabukhina et al. (2018)]. The parameters above imply a line mass of $M_{\rm line} \sim 85\, M_\odot$ pc^{-1}. The critical line mass depends only on gas temperature and mean molecular mass [equation (60) of Ostriker (1964)], thus the 18-K gas bridges have $M_{\rm crit} \sim 35\, M_\odot$ pc^{-1}. Consequently,

in the absence of support, the gas bridges would be gravitationally unstable.

3.6 A low-velocity gas component seen in absorption

Another interesting feature in the ammonia data became apparent from figure 7; the integrated ammonia spectra produced from the combined inter-core pointings exhibits a tentative absorption signature at the velocity marked by the red line—prompting deeper investigation of ammonia gas near the H II continuum peak. To clarify the case of the suspected absorption signature, we integrated ammonia spectra from a 4 × 2 pointing region, which is spatially consistent with the H II region, to increase the signal-to-noise ratio of the spectrum. The selected regions are indicated by the red rectangle locus in figure 8 (left). The resulting spectra are shown in figure 8 (right) for the ammonia (1, 1) and (2, 2) gas.

The integrated spectra show a clear absorption signature in both the (1, 1) and (2, 2) gas; no absorption was seen in the (3, 3) transition. To test whether this could be an artifact caused by the presence of weak ammonia emission in the reference OFF-point, we integrated spectra from the S235AB region, which is not associated with an extended H II region. A contaminated OFF-point would affect all
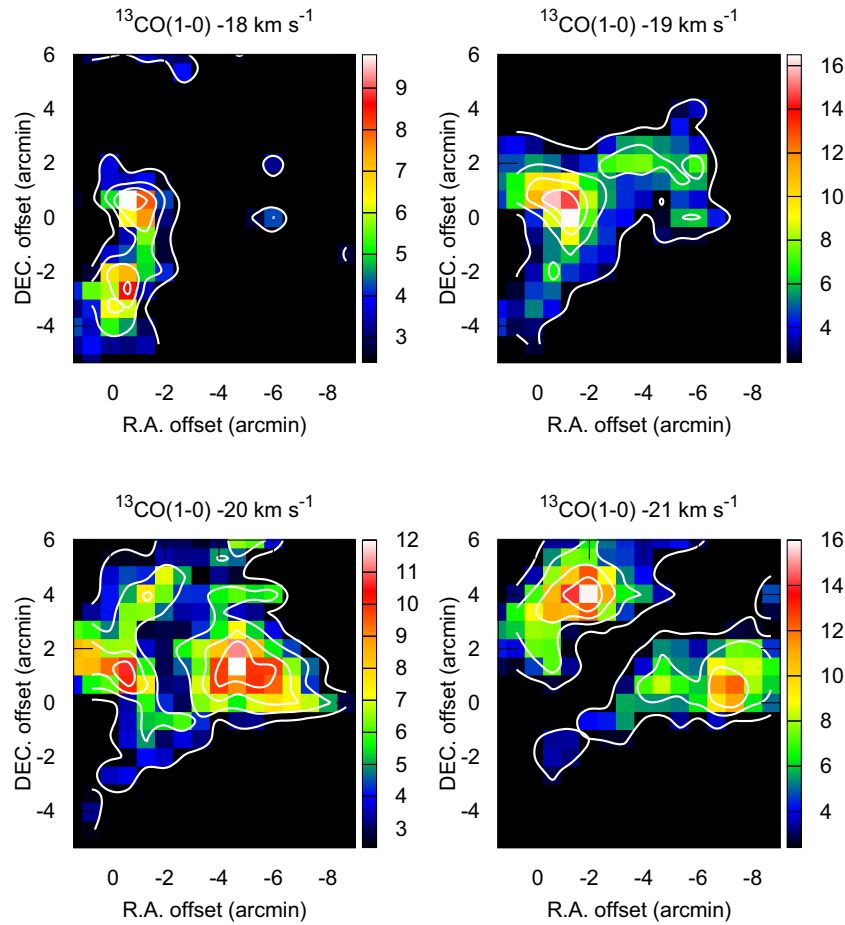
Fig. 5. Re-imaged ^{13}CO data of S235 (excluding S235AB) from Kirsanova et al. (2008) where colour indicates brightness temperature, T_b. Coordinate offsets match those of the ammonia maps. (Color online)

map points in our observations (both S235 and S235AB) equally, however no such absorption signature was found in the integrated S235AB spectrum, supporting the authenticity of the ammonia absorption near the S235 H II region.

From the integrated spectrum we derive a brightness, peak velocity, and velocity half width at half-maximum of $T_b = 0.17 \pm 0.01\,\mathrm{K}$, $v_{\mathrm{LSR}} = -21.07 \pm 0.08\,\mathrm{km\,s^{-1}}$, and $\Delta v_{\mathrm{HWHM}} = 1.29 \pm 0.10\,\mathrm{km\,s^{-1}}$ in emission, and $T_b = 0.07 \pm 0.02\,\mathrm{K}$, $v_{\mathrm{LSR}} = -16.89 \pm 0.14\,\mathrm{km\,s^{-1}}$, and $\Delta v_{\mathrm{HWHM}} = 0.59 \pm 0.02\,\mathrm{km\,s^{-1}}$ for the absorbing gas. The two gas components are sufficiently separated in velocity such that their spectral profiles do not interfere significantly.

Compared to individual points in the searched region, the absorption signature was *enhanced* when multiple pointings were integrated, indicating that the absorbing gas component has an extent that is larger than a single beamsize. As such we rule out interpretations that invoke compact sources of localized absorption of foreground gas on a background of line emission (such as a P-Cygni profile). Instead, an interpretation involving two distinct ammonia gas components is preferred; one at $-17\,\mathrm{km\,s^{-1}}$,

seen in absorption, and one at $-21\,\mathrm{km\,s^{-1}}$, seen in emission. A similar scenario with more clearly defined spectra is shown by (Wilson et al. 1978), who also reach an interpretation of multiple extended gas components. The production of either an emission or an absorption line signature must come from differences in the properties of the gas components themselves, i.e., $T_{\mathrm{line}(-17\,\mathrm{km\,s^{-1}})} < T_{\mathrm{cont}} < T_{\mathrm{line}(-21\,\mathrm{km\,s^{-1}})}$. Here, T_{cont} is the continuum brightness temperature and T_{line} is the brightness temperature of molecular line emission, the velocity of which is indicated in subscript parentheses.

The brightness temperature of the continuum emission cannot be obtained directly from our data because all spectra required spectral baseline fitting during the data reduction stage. As such we must estimate T_{cont} based on observations reported in the literature. First, we estimate the optical depth of the continuum emission at the frequency of our ammonia observations via $\tau = 3.28 \times 10^7 (T_e)^{-1.35}(\nu)^{-2.1}(EM)$. Where T_e is the electron temperature, typically taken as $10000\,\mathrm{K}$ for H II regions, ν is set to the ammonia $(1, 1)$ transition frequency, $22.6914\,\mathrm{GHz}$,
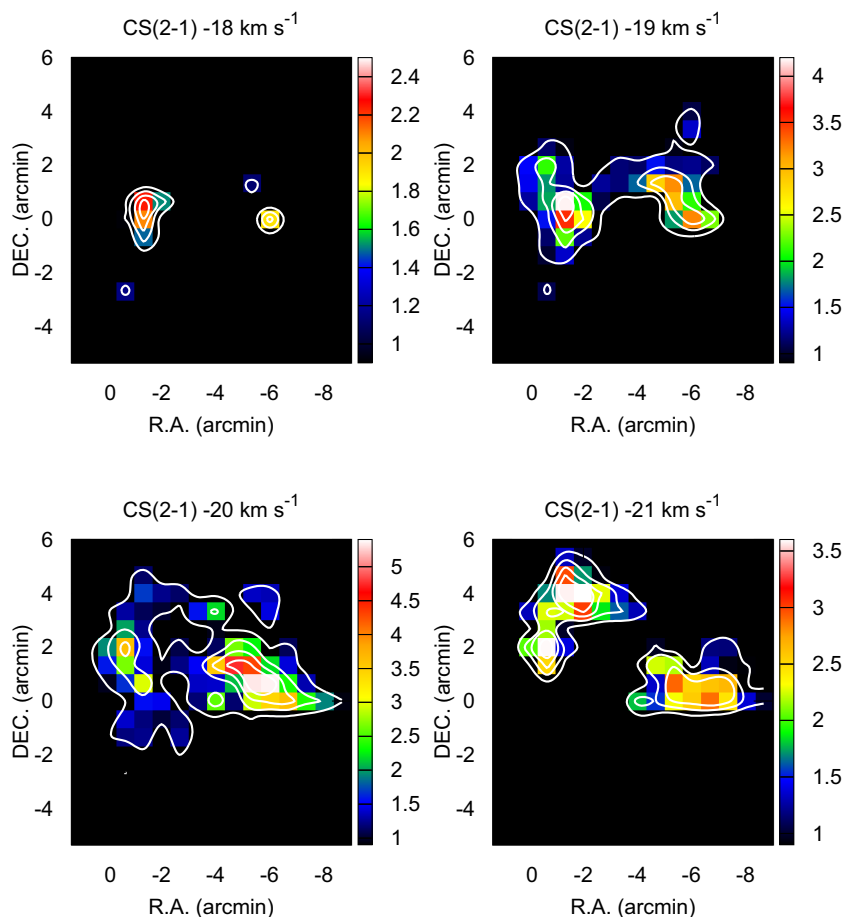
Fig. 6. Re-imaged CS data of S235 (excluding S235AB) from Kirsanova et al. (2008) where colour indicates brightness temperature, T_b. Coordinate offsets match those of the ammonia maps. (Color online)
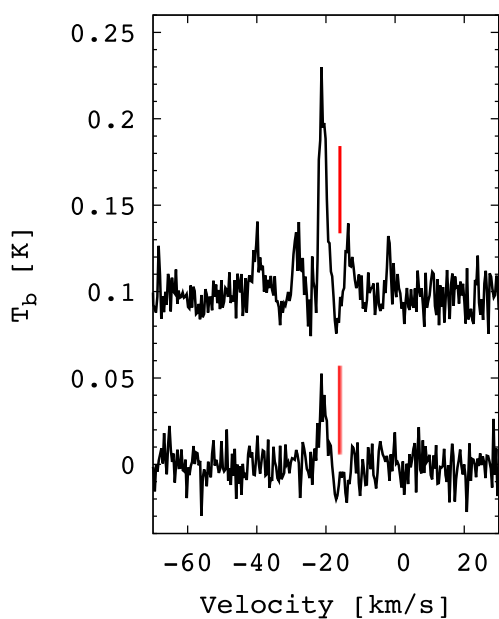

Fig. 7. Integrated spectra of inter-core ammonia gas, showing the (1, 1) transition (above) and the (2, 2) transition (below). (Color online)

and EM is the emission measure. The brightness temperature of the continuum emission can then be estimated using $T_b = T_e(1 - e^{-\tau})$.

Israel and Felli (1978) find an emission measure of S235 of $EM = 0.8 \times 10^4 \, \text{pc cm}^{-6}$ by observations at 1415 MHz with the Westerbork interferometer. On the other hand, Silverglate and Terzian (1978) calculated $EM = 3.7 \times 10^4 \, \text{pc cm}^{-6}$ at 2371 MHz using the 305-m telescope at Arecibo. Employing values from Israel and Felli and from Silverglate and Terzian, respectively, we estimate a range of brightnesses of $T_b = 0.036$ and $0.17 \, \text{K}$ for the continuum emission in S235; the intermediate brightness temperature of the continuum emission is capable of explaining the detection of both emission and absorption of ammonia in S235 for the (1, 1) transition.

The brightness temperatures of the (2,2) transition lines were $T_b = 0.07 \pm 0.01 \, \text{K}$ in emission and $T_b = 0.04 \pm 0.01 \, \text{K}$ in absorption. Repeating the continuum brightness calculations at the frequency of the (2, 2) emission, 23.722 GHz, gives a range of $T_b = 0.034$ to $0.157 \, \text{K}$. Although the range of values of T_{cont} is consistent with
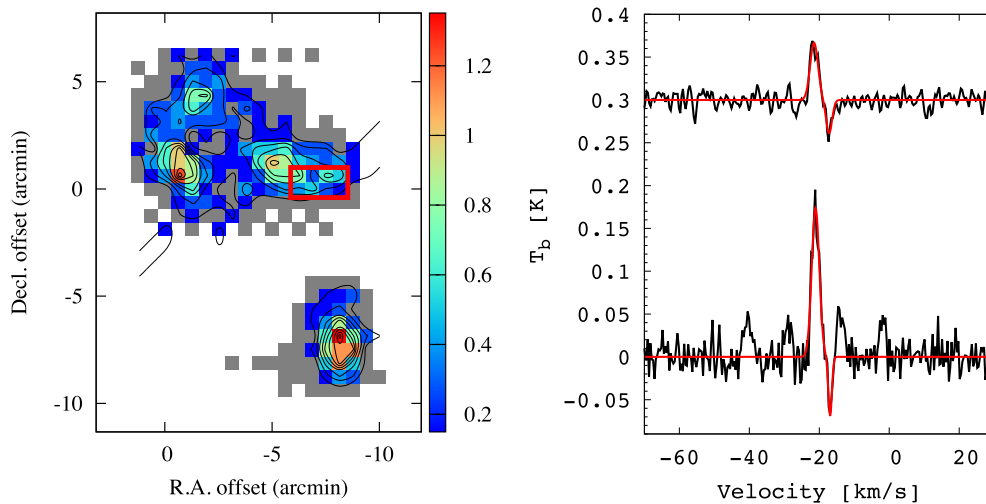
Fig. 8. Left: Region of points included in the integrated spectrum analysis of the absorption signature, highlighted with a red rectangle. Right: Integrated spectra of (below) ammonia (1, 1) and (above) ammonia (2, 2) gas spatially consistent with the extended H II region. Data were Hanning smoothed with a three-point window. The red line shows Gaussian profiles fitted to the emission and absorption peaks. (Color online)

being able to explain the emission and absorption in the (2, 2) emission, the weaker ammonia (2, 2) emission makes the claim less certain.

Another, more direct conclusion drawn from the presence of an absorption spectrum is that the $-17\,\mathrm{km\,s^{-1}}$ component must be in the foreground. Since the present literature finds consensus regarding the blueshifted emission to be foreground gas, we can confirm the redshifted gas to be a second foreground gas component in S235.

3.7 H$_2$O maser emission: Signposts of star formation

In our observations, water maser emission was detected in E1 and S235AB. No previous records of water maser detections exist for E1, therefore these represent newly detected maser features. Emission spectra are shown in figure 9, where a conversion of $2.7\,\mathrm{Jy\,K^{-1}}$ for the Nobeyama telescope has been applied.

The new maser at in E1 (figure 9, lower) was brightest at map grid $(\alpha, \delta)_{\mathrm{J2000.0}} = (05^\mathrm{h}41^\mathrm{m}31^\mathrm{s}\!.3, +35°50'19''\!.5)$. One 2.6-Jy emission peak was detected at a velocity of $-22.5\,\mathrm{km\,s^{-1}}$, which is consistent with the velocity of the E1 core ammonia gas. At least two more maser velocity components were found at -37.3 and $-41.0\,\mathrm{km\,s^{-1}}$ which are blueshifted with respect to the core gas, having fluxes of 1.0 and 4.7 Jy, respectively. This maser is situated near the most luminous of embedded YSOs in E1 which were identified in the Spitzer spectral energy distributions (SEDs) of Dewangan and Anandarao (2011). Furthermore, the emission spectrum is that of a dominant blue-shifted maser (DBSM). Such maser sources are thought to be associated
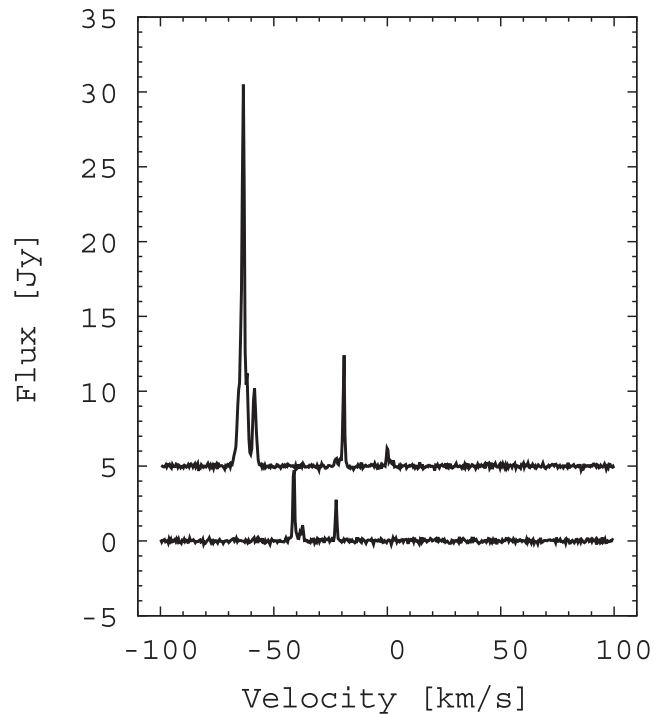
Fig. 9. H$_2$O maser emission detected in E1 (lower) and S235AB (upper).

with jets (Caswell & Phillips 2008; Motogi et al. 2013, 2015; Burns et al. 2015), indicating active star formation.

Maser emission was also detected in the S235AB region (figure 9, upper). The maser in S235AB is also a DBSM source with velocity components near 0, -20, and -60 to $-70\,\mathrm{km\,s^{-1}}$. These maser velocity components were previously catalogued as part of the Medicina patrol discussed in Felli et al. (2007). Water masers in S235AB are known to be associated with massive star formation in that

region and are discussed in the context of multi-epoch very long baseline interferometry (VLBI) observations in Burns et al. (2015).

4 Discussion

4.1 Ammonia emission and absorption: Young and old gas components in S235

The absorption signature discussed in subsection 3.6 suggests the presence of two velocity components of molecular gas; that seen in emission at $-21\,\mathrm{km\,s^{-1}}$ and that seen in absorption at $-17\,\mathrm{km\,s^{-1}}$. Since the differences in emission/absorption come from the physical properties of the gas we can infer that the $-17\,\mathrm{km\,s^{-1}}$ component has a lower excitation temperature than the $-21\,\mathrm{km\,s^{-1}}$ component. The large-scale molecular gas cloud in which S235 is embedded has a velocity of $-16\,\mathrm{km\,s^{-1}}$ (Heyer et al. 1996; Kirsanova et al. 2008). In agreement with the conclusions of Kirsanova et al. (2014), we speculate that the $-17\,\mathrm{km\,s^{-1}}$ absorbing gas component represents the remnants of the progenitor cloud, existing prior to- and yet uninfluenced by the formation of the H II region—hence its low brightness temperature, opacity, and density. On the other hand, the relatively enhanced $-21\,\mathrm{km\,s^{-1}}$ component, seen in emission, traces gas that is being heated by interaction with the H II region.

Using $^{12}\mathrm{CO}$ and $^{13}\mathrm{CO}$ line data, Dewangan and Ojha (2017) investigated the molecular boundaries of two clouds associated with the S235 and S235ABC regions, where two velocity components were traced. The region of ammonia absorption co-locates with one intersect of the two CO clouds of Dewangan and Ojha (2017) (see their figures 5 and 6). They also reported active star formation toward these boundaries. The evidence suggests that the two gas components seen in ammonia may have been involved in a previous CCC event.

4.2 Star formation activity traced by water maser emission

Our observations detected two sites of water maser emission, one of which was a new detection. Water masers indicate that E1 and S235AB are active sites of star formation. This is not surprising, as these cores have been discussed extensively in the context of their star formation activity in several previous publications (Kirsanova et al. 2008, 2014; Dewangan & Anandarao 2011; Dewangan et al. 2016). The maser detections are consistent with the view that both cores are relatively young members of the complex, and they open the opportunity to perform further high-resolution VLBI studies of the star formation activity in E1.

4.3 Ammonia gas bridges as remnants of induced fragmentation

The induction of recent star formation in S235 via the influence of the expanding H II region has been explored and supported by several previous works (Kirsanova et al. 2008; Dewangan et al. 2016; Bieging et al. 2016). To supplement these previous works without repeating them, we concentrate our discussion on the inter-core gas discovered in our observations to consider what appear to be gas remnants of triggered fragmentation.

Inter-core gas bridges were reported in Salii et al. (2002), and were first seen in the S235 star-forming region in Dewangan and Ojha (2017) who report a broad bridge feature of CO gas. Such features (seen in PV) can be produced via the CCC process REF. Dewangan and Ojha (2017) also discuss CCC as a possible formation scenario in the S235 and S235ABC complex.

While optically thin CO gas traces regions of high column density, ammonia emission has a higher critical density and thus traces high-density gas. Our observations reveal the presence of dense molecular gas bridging the cluster-forming gas cores in S235. In the channel maps (figure 2), gas bridges exhibit a typical width of 1.5 times the grid spacing, i.e., $\geq 50''$ wide (0.4 pc at a distance of 1.56 kpc). The first moment map (figure 3) reveals smooth velocity transitions between the cores, indicating a continuous physical link between all four cores. The same structures can be seen in the $^{13}\mathrm{CO}$ and CS channel maps (figures 5 and 6) re-imaged from Kirsanova et al. (2008), further supporting this view.

Low-excitation ammonia (1, 1) is detected in both cores and inter-core bridges, while (2, 2) and (3, 3) emission is more prominent in the cores. The presence of higher-excitation ammonia in the cores indicates that the molecular gas has reached higher column densities and temperatures, suggestive of contraction and internal heating from the resulting star formation. The cold gas bridges seen in ammonia show no indication of star formation activity, as is supported by the lack of inter-core stellar density enhancements (Dewangan & Anandarao 2011). This is reflected in our integrated spectral analyses in subsection 3.5 which reveal that the inter-core bridges comprise gas of lower temperature and column density than core gas.

Dust filaments bearing some resemblance to those discussed here are seen at smaller scales with a characteristic width of $\sim 0.1\,\mathrm{pc}$, in which cores house individual protostars. The configuration, commonly described as "pearls on a string," was initially seen in infrared data from the Herschel space telescope (Arzoumanian et al. 2011) and has since been recognized as a common feature of star formation. On the other hand, filaments of much larger

scales have been found in other star-forming regions such as NGC 6334 (Zernickel et al. 2013), and gas bridges of a similar scale to those in S235 connect multiple developed H II regions in OMC-1 (Hacar et al. 2017) and the large filament observed in molecular gas in WB 673 (Kirsanova et al. 2017). However, the nature of the aforementioned filamentary systems differs markedly from those seen in S235, which instead connect *clusters* of YSOs rather than individual protostars, and have formed in the presence of—and by interaction with—a single H II region. Additionally, analysis of the dense gas physical parameters implies hypercritical line masses, highlighting the potential for further star formation.

Our interpretation is that the quiescent physical gas bridges linking the cores are the remnants of a large-scale fragmentation process in which the cluster-forming cores of S235 condensed out of a single parent molecular cloud. Further evidence of the existence of a natal gas component comes by way of the absorption feature discussed above. Whether the fragmentation of the parent cloud was driven by CCC, C&C, or RDI should therefore be considered. Whitworth et al. (1994) showed that the swept-up gas layers of expanding nebulae, winds, and CCCs were likely to collapse, by gravitational instability, to form massive cores of gas. Furthermore, Walch et al. (2015) showed that C&C and RDI caused by an expanding H II region are capable of producing a shell-like structure studded with cores. Their simulations produce a configuration of bridged gas cores similar to those seen in this work.

On the scale of the larger S235ABC complex, Dewangan and Ojha (2017) revealed evidence of CCC as a likely trigger of the subsequent star formation seen in this region. Dewangan et al. (2016) showed pressure from the expanding H II region to be the dominant driver of gas dynamics in the S235 main, capable of explaining the formation of E2, CE, and CW (see their subsection 3.7), remarking that the youngest core, E1, may be better explained by RDI [a similar conclusion was also reached by Kirsanova et al. (2014)].

Considering our result in the context of these works, we conclude that the ammonia gas bridges found in S235 likely represent the hyper-critical remnants of CCC-induced fragmentation of a gas cloud involving the C&C mechanism with likely contribution from the RDI process. Both processes contribute to the proliferation of triggered star formation, driven by the central H II region of S235.

5 Conclusions

The main conclusions of this paper can be summarized as follows:

- We performed position-switch mapping observations of the S235 and S235AB regions in ammonia (1, 1), (2, 2), (3, 3), and the 22-GHz water maser transition using the Nobeyama 45-m radio telescope.
- Our observations determined the physical properties of molecular gas in the cores of this SFR, which agree with, and expand on, the previous works in the literature.
- Focusing on the less-studied gas away from the cores, our observations uncovered the presence of gas bridges that link the cluster-forming cores in the S235 region. These bridges appear to be remnants of a fragmentation event which led to the formation of its present-day cores from a larger parent cloud. This fragmentation was likely driven by the impact of the extended H II region S235 to surrounding molecular cloud.
- The presence of dense gas bridges was corroborated by CS and ^{18}CO gas maps, re-imaged from Kirsanova et al. (2008).
- Further relic gas was detected in absorption at the foreground of the radio continuum peak in S235 at a velocity consistent with the local diffuse molecular cloud. Thus there are two ammonia gas components in the S235 region: old quiescent gas of low brightness temperature (seen in absorption) and younger, more active star-forming gas which is seen to interact with the H II region (seen in emission).
- Our study detected strong water masers associated with star formation in S235AB and the E1 core of S235, the latter being a new maser detection.

Acknowledgments

References

Arzoumanian, D., et al. 2011, A&A, 529, L6

Bieging, J. H., Patel, S., Peters, W. L., Toth, L. V., Marton, G., & Zahorecz, S. 2016, ApJS, 226, 13

Burns, R. A., Imai, H., Handa, T., Omodaka, T., Nakagawa, A., Nagayama, T., & Ueno, Y. 2015, MNRAS, 453, 3163

Caswell, J. L., & Phillips, C. J. 2008, MNRAS, 386, 1521

Chibueze, J. O., et al. 2013, ApJ, 762, 17

Dewangan, L. K., & Anandarao, B. G. 2011, MNRAS, 414, 1526

Dewangan, L. K., & Ojha, D. K. 2017, ApJ, 849, 65

Dewangan, L. K., Ojha, D. K., Luna, A., Anandarao, B. G., Ninan,

J. P., Mallick, K. K., & Mayya, Y. D. 2016, ApJ, 819, 66

Elmegreen, B. G. 1998, in ASP Conf. Ser., 148, Origins, ed. C. E. Woodward et al. (San Francisco: ASP), 150

Elmegreen, B. G., & Lada, C. J. 1977, ApJ, 214, 725

Felli, M., et al. 2007, A&A, 476, 373

Friesen, R. K., et al. 2017, ApJ, 843, 63

Georgelin, Y. M., Georgelin, Y. P., & Roux, S. 1973, A&A, 25, 337

Habe, A., & Ohta, K. 1992, PASJ, 44, 203

Hacar, A., Alves, J., Tafalla, M., & Goicoechea, J. R. 2017, A&A, 602, L2

Harju, J., Walmsley, C. M., & Wouterloot, J. G. A. 1991, A&A, 245, 643

Haworth, T. J., et al. 2015a, MNRAS, 450, 10

Haworth, T. J., Glover, S. C. O., Koepferl, C. M., Bisbas, T. G., & Dale, J. E. 2018, Nature, 82, 1

Haworth, T. J., Shima, K., Tasker, E. J., Fukui, Y., Torii, K., Dale, J. E., Takahira, K., & Habe, A. 2015b, MNRAS, 454, 1634

Heyer, M. H., Carpenter, J. M., & Ladd, E. F. 1996, ApJ, 463, 630

Ho, P. T. P., & Townes, C. H. 1983, ARA&A, 21, 239

Inutsuka, S.-i., & Miyama, S. M. 1997, ApJ, 480, 681

Israel, F. P., & Felli, M. 1978, A&A, 63, 325

Kennicutt, R. C., Jr 1998, ApJ, 498, 541

Kirsanova, M. S., Salii, S. V., Sobolev, A. M., Olofsson, A. O. H., Ladeyschikov, D. A., & Thomasson, M. 2017, Open Astron., 26, 99

Kirsanova, M. S., Sobolev, A. M., Thomasson, M., Wiebe, D. S., Johansson, L. E. B., & Seleznev, A. F. 2008, MNRAS, 388, 729

Kirsanova, M. S., Wiebe, D. S., Sobolev, A. M., Henkel, C., & Tsivilev, A. P. 2014, MNRAS, 437, 1593

Ladeyschikov, D. A., Kirsanova, M. S., Tsivilev, A. P., & Sobolev, A. M. 2016, Astrophys. Bull., 71, 208

Millar, T. J., Farquhar, P. R. A., & Willacy, K. 1997, A&AS, 121, 139

Motogi, K., et al. 2015, PASJ, 68, 69

Motogi, K., Sorai, K., Niinuma, K., Sugiyama, K., Honma, M., & Fujisawa, K. 2013, MNRAS, 428, 349

Nakano, M., et al. 2017, PASJ, 69, 16

Nguyen-Luong, Q., et al. 2016, ApJ, 833, 23

Ostriker, J. 1964, ApJ, 140, 1056

Ruoskanen, J., Harju, J., Juvela, M., Miettinen, O., Liljeström, A., Väisälä, M., Lunttila, T., & Kontinen, S. 2011, A&A, 534, A122

Ryabukhina, O. L., Zinchenko, I. I., Samal, M. R., Zemlyanukha, P. M., Ladeyschikov, D. A., Sobolev, A. M., Henkel, C., & Ojha, D. K. 2018, Res. Astron. Astrophys., 18, 095

Salii, S. V., Sobolev, A. M., & Kalinina, N. D. 2002, Astron. Rep., 46, 955

Sandford, M. T., II, Whitaker, R. W., & Klein, R. I. 1982, ApJ, 260, 183

Schmidt, M. 1959, ApJ, 129, 243

Silverglate, P. R., & Terzian, Y. 1978, ApJ, 224, 437

Torii, K., et al. 2017, ApJ, 835, 142

Toujima, H., Nagayama, T., Omodaka, T., Handa, T., Koyama, Y., & Kobayashi, H. 2011, PASJ, 63, 1259

Walch, S., Whitworth, A. P., Bisbas, T. G., Hubber, D. A., & Wünsch, R. 2015, MNRAS, 452, 2794

Walmsley, C. M. 1994, in AIP Conf. Proc., 312, Molecules and Grains in Space, ed. I. Nenner , (New York: AIP) 463

Whitworth, A. P., Bhattal, A. S., Chapman, S. J., Disney, M. J., & Turner, J. A. 1994, MNRAS, 268, 291

Wilson, T. L., Bieging, J., & Downes, D. 1978, A&A, 63, 1

Wu, G., Qiu, K., Esimbek, J., Zheng, X., Henkel, C., Li, D., & Han, X. 2018, A&A, 616, A111

Zernickel, A., Schilke, P., & Smith, R. J. 2013, A&A, 554, L2